npj | Climate and Atmospheric Science

www.nature.com/npjclimatsci

ARTICLE OPEN

Check for updates

Moisture channels and pre-existing weather systems for East Asian rain belts

Tat Fan Cheng[1], Mengqian Lu[1]✉ and Lun Dai[1]

Rain belts in East Asia frequently pose threats to human societies and natural systems. Advances in a skillful forecast on heavy precipitation require a deeper understanding of the preconditioned environments and the hydrologic cycle. Here, we disentangle 15 dominant moisture channels along four corridors reaching the Somali Jet, South Asia, Bay of Bengal, and Pacific basin for the warm-season rain belts. Among them, the Somali and South Asian channels were underappreciated in the literature. The results also highlight the importance of terrestrial moisture sources, and the close relationship between the moisture pathways and rain belts' characteristics. Back-tracing the weather within a 2-week lead time reveals the pre-existing weather systems and circumglobal wave trains, that govern the moisture channels. Findings from this work develop a better understanding of East Asian rain belts' water cycle, and may offer insights into model evaluation and heavy rainfall prediction at a longer lead time.

npj Climate and Atmospheric Science (2021)4:32 ; https://doi.org/10.1038/s41612-021-00187-6

INTRODUCTION

Being the most influential and iconic weather phenomenon during the East Asian summer monsoon (EASM) season, the east-west elongated rain belts often trigger landslides and floods that greatly disrupt agriculture, natural systems, and human properties. These rain belts exhibit a northward migration on the intraseasonal time scale, which orchestrates distinct monsoon stages in various parts of East Asia, such as the Pre-Meiyu, Meiyu/Baiu and mid-summer stages[1–4]. Intensive efforts have been devoted to study the immediate causes of the rain belt formation and distributions at the local scale[5,6], such as the super-geostrophic lower-level jets[7,8], strong horizontal shear lines[9], sharp gradients of equivalent potential temperature[10], and the upper-level westerlies[11,12]. There has also been growing attention towards the processes that cause extreme continental precipitation in East Asia on a 2-week time scale, such as non-local moisture sources, moisture transport, and the teleconnected weather circulations[13–17] and that in other places of the world[18–21]. We saw intensive endeavors to establish the source–receptor network to better understand the dominant sources for monsoon rainfall over continents[13,14,22,23].

In terms of moisture transport, four main pathways have been widely recognized to supply moisture to summer precipitation in East Asia, including those from the Bay of Bengal, South China Sea, western North Pacific, and Eurasia[14,24–28]. Early studies on major moisture pathways were conducted mainly through numerical experiments on moisture influx to the target region[25] or moisture budget diagnosis from the Eulerian perspective[26–28]. A recent study[24] revealed the main moisture channels that were similar to those documented in early studies using the Hybrid Single-Particle Lagrangian Integrated Trajectory (HYSPLIT) model. Yet, the results largely depended on the choice of prescribed source areas where trajectories were averaged. As multiple lines of evidence suggest that the upwind terrestrial sources and the remote Indian Ocean were important for summer precipitation in East Asia[13,15,23,29], there may exist a discrepancy between the current understandings of the dominant moisture sources and the pathways. For this reason, we recognize the need for revisiting and updating the knowledge about moisture transport through objectively mining the important moisture supply channels that were overlooked in the past. Further, given that forecasting heavy precipitation with lead times beyond 5 days remains challenging for numerical weather models[30,31], a deeper understanding of the preconditioned synoptic-scale environments 2 weeks before heavy rainfall would be beneficial for numerical forecasting at a longer lead time[32–34]. Hence, it is important to holistically depict the moisture pathways and the preconditioned weather systems that govern the hydrologic cycle for East Asian rain belts, which remains a research gap to be filled.

In this study, we perform backward tracking experiments on the moisture from the detected rain belts in East Asia during the warm season (April–September) using a semi-Lagrangian dynamical recycling model (DRM)[35,36]. We classify up to 15 moisture channels for all the events using a data-driven trajectory clustering method (see "Methods" section), and reveal the connections between the characteristics of rain belt events and the moisture channels. Based on the dominant moisture channels, we diagnose the key weather regimes that govern the moisture channels up to 2 weeks ahead, which would be useful sources of predictability for East Asian rain belts. This study will help fill the missing pieces of the atmospheric water cycle for the East Asian rain belts, and offer insights on the key weather patterns and teleconnections that may increase the lead time for heavy rainfall forecasts.

RESULTS

Four main moisture corridors

We begin by presenting 15 clusters of moisture channels, with the majority stacked along four main corridors for East Asian rain belts (Fig. 1a). These corridors include the Somali corridor (S1 and 2), the South Asian corridor (SA1–4), the Bay of Bengal corridor (B1–3) and the Pacific corridor (P1–3). The "least popular" corridor (i.e., the Somali corridor) accounts for ~11% of the moisture trajectories tracked from the EASM rain belt events, while the "most popular" one (i.e., the South Asian corridor) covers ~29% of the trajectories in the warm season. The four corridors altogether

[1]Department of Civil and Environmental Engineering, The Hong Kong University of Science and Technology, Hong Kong, China. ✉email: mengqian.lu@ust.hk

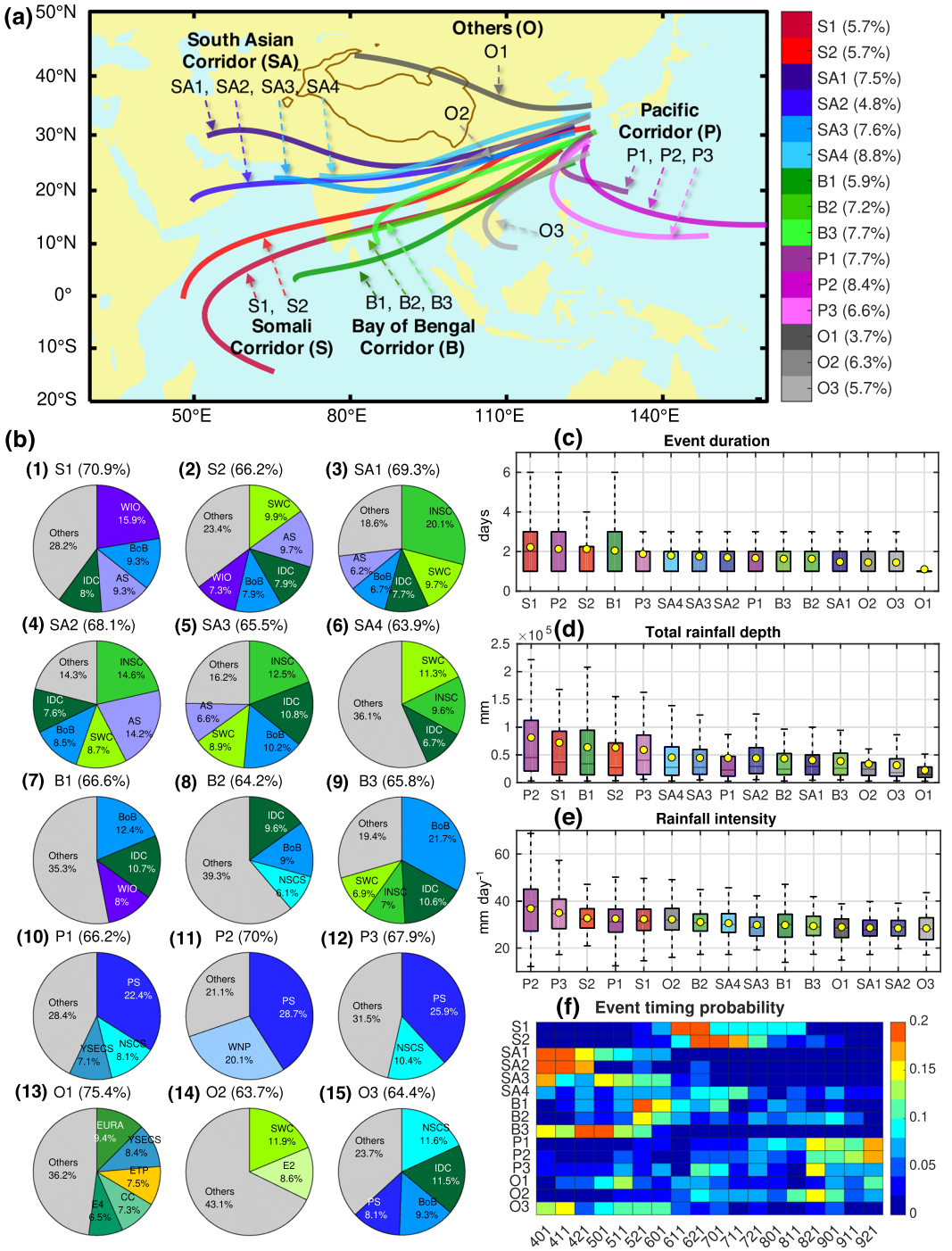

Fig. 1 Spatiotemporal features and moisture sources for the 15 moisture channels. a The regression curves derived from the backward moisture trajectories of the East Asian rain belt events from April through September in 1981–2018. Most moisture channels are labeled according to the corresponding corridors, including Somali corridor (S), South Asian corridor (SA), Bay of Bengal corridor (B), and Pacific corridor (P). Other types of channels are labeled with an O. Numbers in the parentheses aside the color bar show the percentages of trajectories (~1 million) assigned to individual clusters. **b** Pie charts of different sources' contributions to rain belt events assigned to each moisture channel. Sources with contributions greater or equal to 6% are labeled with the acronyms, while the rest are grouped into the category "Others". The definition of acronyms can be found in the caption of Supplementary Fig. 1. The total attributed fractions of precipitation are shown in the subtitles. **c** Box plots of duration (unit: day), **d** total rainfall depth (unit: mm) and **e** rainfall intensity (unit: mm day^{-1}) of rain belt events in each cluster. The boxplots are the traditional ones with the bars representing the maximum, 75th quantile, median, 25th quantile, and minimum. All boxplots are sorted in descending order of the mean (denoted by a yellow dot). **f** Heatmap of the arrival timings of rain belt events in each cluster in terms of probability. The number "401" in the *x*-axis denotes a dekad (i.e., 10 days) from April 1 to 10, and a similar convention applies to other values.

cover ~84% of the moisture trajectories that supply the warm-season rain belts in East Asia. While the Somali corridor was believed to affect East Asian summer rainfall in some of the previous studies[27,37], the South Asian corridor was rarely documented but is crucial for supporting East Asian rain belts in the warm season, as suggested here.

Apart from the main corridors, there are secondary channels from the mid-latitudes, inland East Asia, and the South China Sea. Surprising as it may seem, the South China Sea channel (O3) only accounts for ~6% of the moisture trajectories, suggesting that such a traditionally known moisture channel turns out to be minor for East Asian rain belts. This finding is consistent with our previous study that the South China Sea plays a secondary role in the warm-season precipitation in South China and the mid-lower Yangtze river basin[13]. It is worth mentioning that there is no cross-equatorial moisture channel from Australia as proposed by early studies[3,37], implying that the direct moisture transport from the southern hemisphere might be trivial. This possibly results from the weak meridional flow across Maritime islands[27], the deflection of airflows by the Coriolis force[38] and the ascendency of the southwest Indian monsoons and the western North Pacific subtropical high (WNPSH)[13,39].

Among the four dominant corridors, the Somali corridor manages the longest moisture channels (i.e., S1 and 2) from the remote western Indian Ocean, where the Somali jet prevails in the warm season. As such, the Somali channels sequentially uptake water vapors from the western Indian Ocean, the Arabian Sea, the Bay of Bengal, Indochina and even Southwest China (Fig. 1b(1)–(2)). Owing to a shorter pathway of the Bay of Bengal channels (B1–3), strong moisture uptake is mainly over the Bay of Bengal and Indochina (Fig. 1b(7)–(9)). The difference in the lengths of the Somali and the Bay of Bengal channels, as we will show later, reveals distinctive weather regimes at play (see "SAL-WNPSH coupling" and "Western extension of the WNPSH" sections). In contrast, the Pacific corridor carries abundant moisture from the Philippine Sea, Western North Pacific, and Northern South China Sea (Fig. 1b(10)–(12)). The South Asian corridor, instead, primarily collects terrestrial moisture from the interior continent, including the Indian subcontinent, Southwest China, and Indochina (Fig. 1b (3)–(6)). We find it intriguing that 7 out of the 15 channels rely more on terrestrial sources than the oceans (Supplementary Fig. 2). This finding reveals the conspicuous role of upwind terrestrial sources in the downwind rain belts during the EASM season, as also supported by recent research[13,29,40,41]. It should be noted that around one-third of the rain belt precipitation is left unattributed in the DRM (Fig. 1b), possibly due to the fast recycling process and the inherent well-mixed constraint in the model[35,42]. That said, the leading sources mentioned above are likely to stay the same if the moisture attribution ratio becomes higher.

Moisture channels and rain belt characteristics

We see a quite remarkable disparity in the strength and persistence of rain belt events fed by different types of moisture channels. Statistically, long-range oceanic channels, including the S1, S2, B1, and P2 channels, are associated with relatively persistent rain belt events with a mean lifetime greater than 2 days (Fig. 1c). Those persistent events are also the ones that produce high total rainfall depths (i.e., the accumulated precipitation of a rain belt event throughout its lifetime) (Fig. 1d), posing a great hydrologic threat to East Asia. As will be shown later, the long-range channels from the Indian basin are driven by prominent and well-organized weather systems, which continuously steer strong monsoonal airflows or even the atmospheric rivers[16,17,21] to sustain the East Asian rain belts. In addition, the Pacific channels (e.g., P2 and P3) contribute water vapors to rain belt events that have a relatively high rainfall intensity (Fig. 1e), due to tropical cyclone activities in the western Pacific basin[13] (see "Tropical cyclones and eastward retreat of the WNPSH" section). Conversely, those scattered and short-range channels from the mid-latitudes (O1), inland East Asia (O2), and the South China Sea (O3) are mostly associated with shorter and somewhat trivial rain belt events (Fig. 1c, d). It may be surprising to know that the South Asian channels fed by terrestrial sources are related to rain belt events with moderate duration, total rainfall depth, and intensity (Fig. 1c–e). This finding, again, underscores the role of terrestrial moisture channels in sustaining East Asian rain belts.

We also note that the arrival time of the rain belt events fed by the same moisture corridor tends to synchronize. Specifically, the South Asian channels more actively partake in rain belt events from April to mid-May (Fig. 1f), when the Spring stage in East Asia prevails[2,43]. Following them, events fueled by the Bay of Bengal channels (B1–3) tend to appear in the Pre-Meiyu stage from early-May to early-June[1]. Progressing into the Meiyu season (mid-June to mid-July)[44], we see stronger and more persistent rain belt events dominated by the Somali channels (S1 and 2). This is also the time when the Somali jets, the Indian summer monsoon and the EASM all peak in their strengths[45,46]. Events of the Pacific channels (P1–3), in contrast, are inclined to occur during the typhoon season (i.e., late summer). The unexpectedly clean cut in the arrival time of events of different moisture corridors reflects the prominent seasonality of both the rain belt's water cycle and the Asian weather system.

Governing weather systems and teleconnections

Given the pronounced seasonality of the moisture corridors, it is meaningful to explore the weather systems and teleconnections that set up the corridors in the first place. In the following sections, we unfold several pre-existing weather systems that lay the moisture channels 2 weeks ahead of the rain belt events based on weather composites. We organize the results around the key weather regimes that govern different moisture channels in similar periods of the season for ease of comparison and generalization of important weather systems. Different lead-time settings are chosen in composite maps to present the weather systems' evolution better. The anomaly fields shown in the composites are the mean deviations of daily fields from the 5-day-moving-mean daily climatology (1981–2018).

SAL-WNPSH coupling

One of the most interesting weather patterns involves two canonical circulations during the Asian summer monsoon season––the South Asian low (SAL) and the western North Pacific subtropical high (WNPSH). The former draws abundant monsoonal rainfall to South Asia, while the latter assists in the frontogenesis in East Asia[39,47]. The synergistic coupling of these two weather systems favors the long-range Somali channels and a Bay of Bengal channel. Specifically, alongside the S1 channel, we observe a strong SAL accompanied by enhanced Somali jets and the southwest Indian monsoons, expands to East Asia from day −11 to −3 (Fig. 2a–c). Subsequent to the SAL's demise, the WNPSH strengthens and extends westward at 10–20°N (Fig. 2c, d), favoring southwesterly moisture fluxes and frontal convergence over the entire EASM domain. Such a SAL-WNPSH coupling opens a moisture highway by connecting the Somali jets, Indian, and East Asian southwesterly monsoons. We find similar coupled circulations that steer the S2 channel (Fig. 2f–i), yet the difference comes from a northward-positioned SAL that causes S2 to the north of the S1 channel (Fig. 2b, g), and thereby more northward-shifted rain belts (Fig. 2e, j). Noticeably, the B1 channel is steered by a weaker SAL-WNPSH coupling, while the SAL centers in the eastern Bay of Bengal and results in a shorter moisture track (Fig. 2k–n).

The interesting SAL-WNPSH coupling begs the question of how it forms in this way. It turns out that the 200-hPa divergent wind anomalies in the east of the SAL converge over the western North Pacific in all three channels' composites (Supplementary Fig. 3a–c,

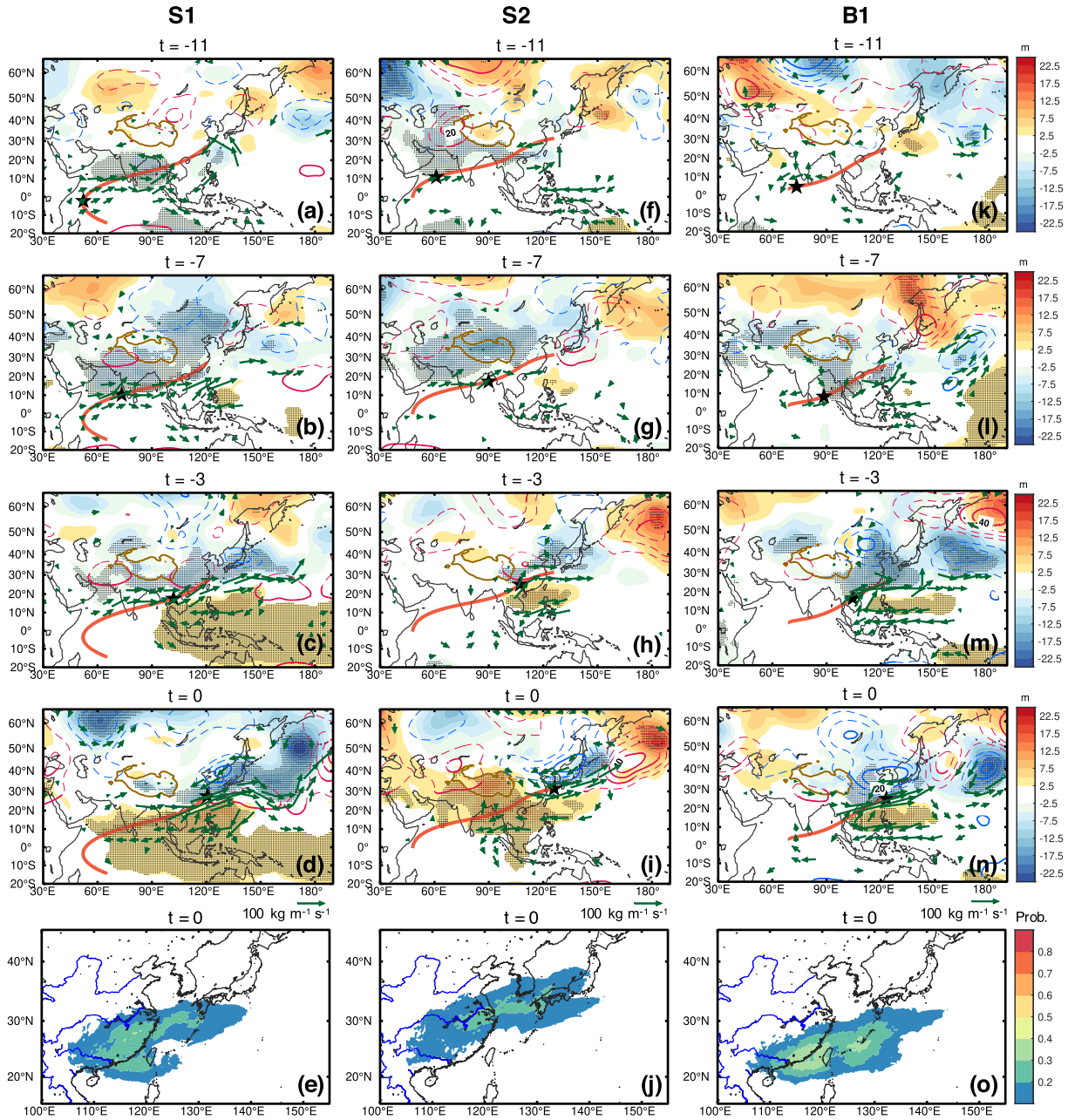

Fig. 2 Composites of meteorological fields within 2 weeks ahead of the clustered events fed by the S1, S2, and B1 channels. a–d The S1 channel's composites of 850-hPa geopotential height anomalies (shading, unit: m), 200-hPa geopotential height anomalies (contour, unit: m) and vertically integrated vapor transport (IVT) anomalies (vector, unit: kg m^{-1} s^{-1}) on day −11, −7, −3 and 0 with respect to the occurrence of rain belt events (95 events), with day 0 being the first day of the event. **e** A risk map of the S1's rain belt occurrence probabilities on day 0. **f–j** Composites and the risk map for the S2 channel (93 events). **k–o** for the B1 channel (78 events). The solid red line represents the regressed moisture channel, along which the black star denotes the regressed position of the moist air column corresponding to the lead time. Contours in red (blue) denote positive (negative) values. Black dots over the shading, thick solid contours and the vectors all indicate statistically significant values at the 0.05 level (Student's *t*-test).

e–g, and j–l). Such an upper-level convergence of airflows would promote the lower-level divergence, and partly explain the subsequent development of the WNPSH.

Notably, the three channels (i.e., S1, S2, and B1) tend to occur in a similar period from late-May to mid-July (Fig. 1f), implying that the observed SAL-WNPSH coupling shares a similar background climatology. As these channels are all related to strong and persistent rain belt events (Figs. 1c, d), the SAL-WNPSH coupling is arguably the key weather regime to initiate the long-range moisture channels, and the strong Pre-Meiyu and Meiyu rain belts in South China and the mid-lower Yangtze river basin (Fig. 2e, j, o).

Dual-anticyclone pattern

Another key coupling is a dual-anticyclone pattern consisting of an anomalous anticyclone in South Asia and the WNPSH, which commonly controls the terrestrial South Asian channels (SA1, 3, and 4) (Fig. 3). Regarding the SA1 channel, for example, we see

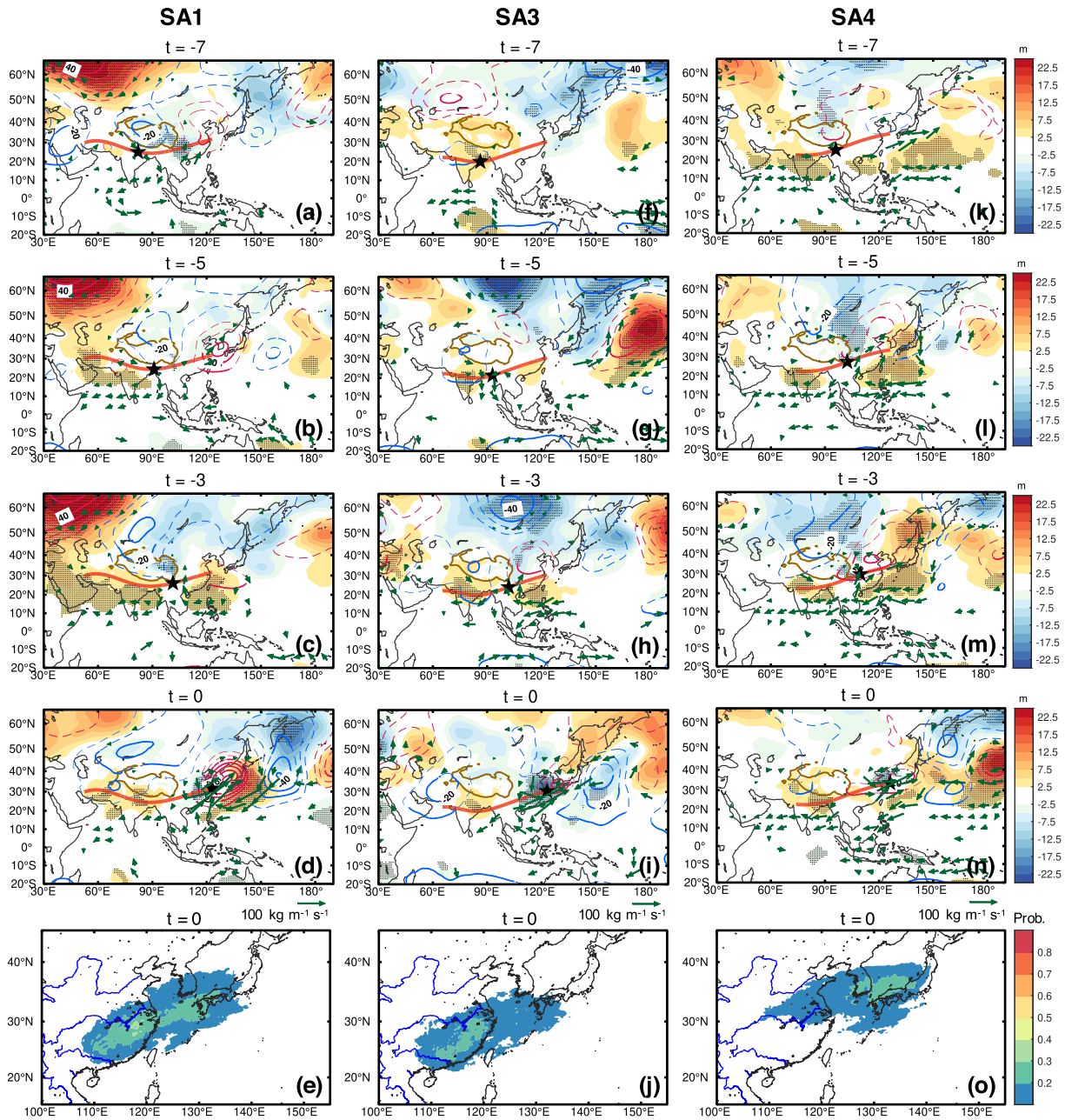

Fig. 3 Composites of meteorological fields within 2 weeks ahead of the clustered events fed by the SA1, 3 and 4 channels. a–e As in Fig. 2, but for SA1 (106 events), **f–j** SA3 (84 events), and **k–o** SA4 (129 events) on day −7, −5, −3, and 0.

prominent easterly IVT anomalies over the northern Indian Ocean on day −7, which later accompany a high-pressure anomaly straddling over the Indian subcontinent and the adjacent seas (Fig. 3a, b). Such an anomalous anticyclone hinders the moisture transport from the Indian Ocean. Subsequent to the South Asian anticyclone, the WNPSH strengthens and steers moisture from the southwest (Fig. 3c, d). The interplay of the two anticyclones effectively blocks the moisture from the Indian Ocean, while maintaining the moisture advection from South Asian land. This observation also explains why the South Asian corridor strongly depends on terrestrial sources (Fig. 1b). We find slightly different strengths and positions of the dual anticyclones in other South Asian channels that explain the nuances in the pathways (Fig. 3f–h, k–n). A similar dual-anticyclone pattern was also identified in our previous work in which it directly correlated with contributions from South Asian land sources[13].

The arrival time of the events gives clues about the timing of the weather pattern. Specifically, the SA4 channel tends to appear from late-June to July, while the other SA channels mainly occur in April and May (Fig. 1f). As such, the dual-anticyclone pattern in the early summer (when the western ridge of the WNPSH mainly resides in the South China Sea[47]) steers the SA1 and 3 channels to induce rain belts to the south of the Yangtze river basin (Fig. 3e, j). In contrast, the dual-anticyclone pattern in the mid-summer consists of a northward-extended WNPSH[47], leading to the SA4 channel that fuels the Baiu-Changma rain bands over the Korean Peninsula and South Japan (Fig. 3o). The finding of the South Asian corridor

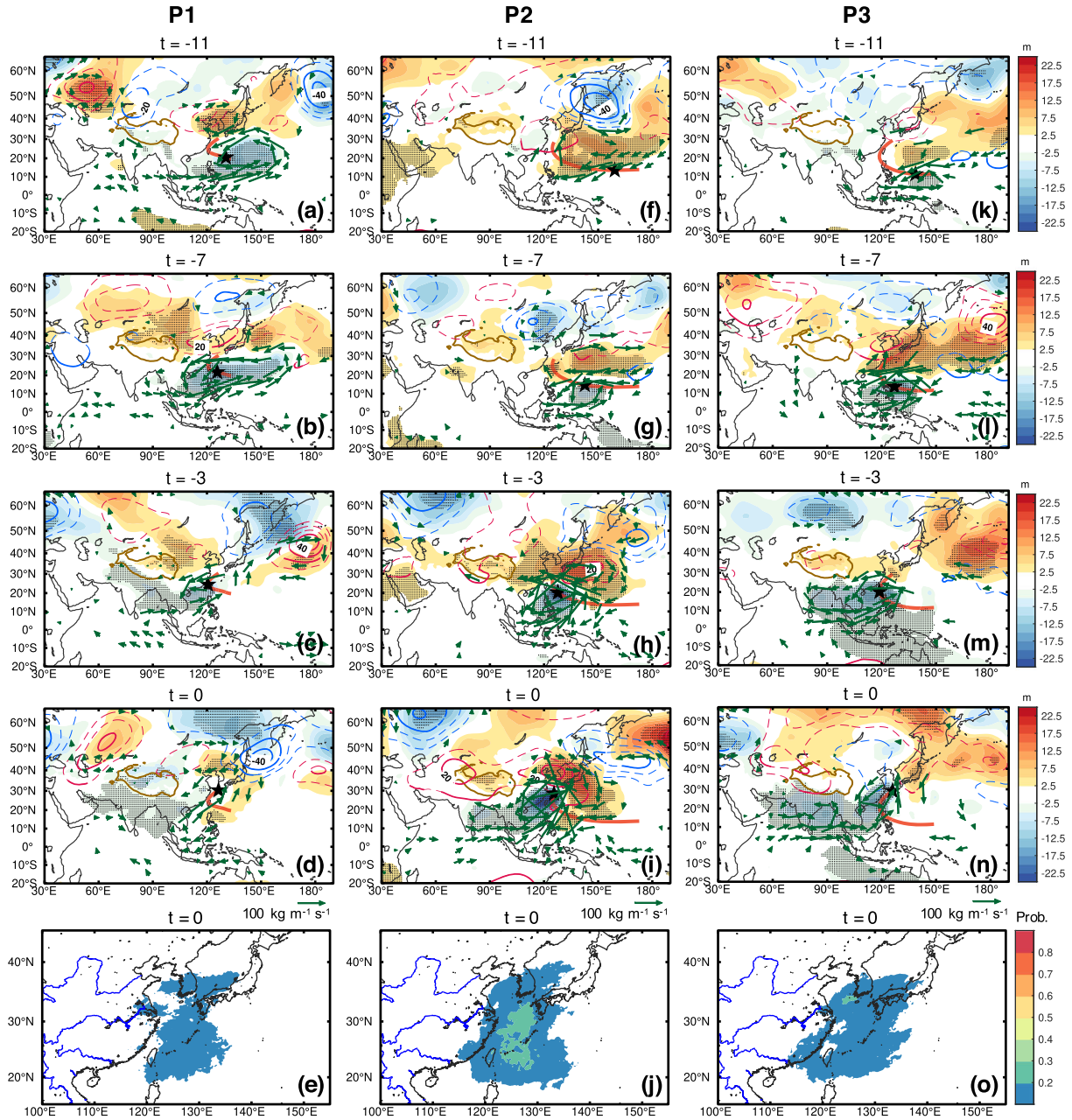

Fig. 4 Composites of meteorological fields within 2 weeks ahead of the clustered events fed by the P1–3 channels. a–e As in Fig. 2, but for P1 (121 events), **f–j** P2 (106 events) and **k–o** P3 (93 events) on day −11, −7, −3, and 0.

certainly improves our understanding of the monsoon rain belts' atmospheric water cycle.

Tropical cyclones and eastward retreat of the WNPSH

The Pacific channels' weather regimes bear some similarities in which an anomalous cyclone emerges over the western Pacific a week before the rain belt events (Fig. 4). As the cyclone propagates northwestward, the accompanied moisture fluxes to its northeast convey abundant moisture from the Pacific Ocean to East Asia (Fig. 4a–d, g–i, and k–m), contributing to intensive rain belts alongshore and over the Eastern China Sea (Fig. 4e, j, o). Further, the best track data (see "Data" section) reveals substantial percentages of rain belt events in P1 (59%), P2 (78%), and P3 (60%) co-occurred with tropical depressions or stronger tropical cyclones (i.e., maximum sustained wind speed exceeding 41 km h^{-1}). This finding confirms the role of tropical cyclones in establishing the Pacific corridor in late summer (Fig. 1f), which explains the relatively high rainfall intensity associated with P2 and 3 channels mentioned earlier (Fig. 1e). As for the differences, P1 is accompanied by a cyclonic anomaly at a larger scale compared with that observed in P2 and 3, occupying the entire western North Pacific basin and propagating slowly to the west (Fig. 4a–d). Such synoptic weather pattern may imply the eastward retreat of the WNPSH in inducing the Pacific channel[39].

Westward extension of the WNPSH

On the contrary, the westward extension of the WNPSH is key to the relatively short-range moisture channels from the Bay of Bengal (B2), inland East Asia (O2), and the South China Sea (O3) (Fig. 5). Unlike the SAL-WNPSH coupling and the dual-anticyclone

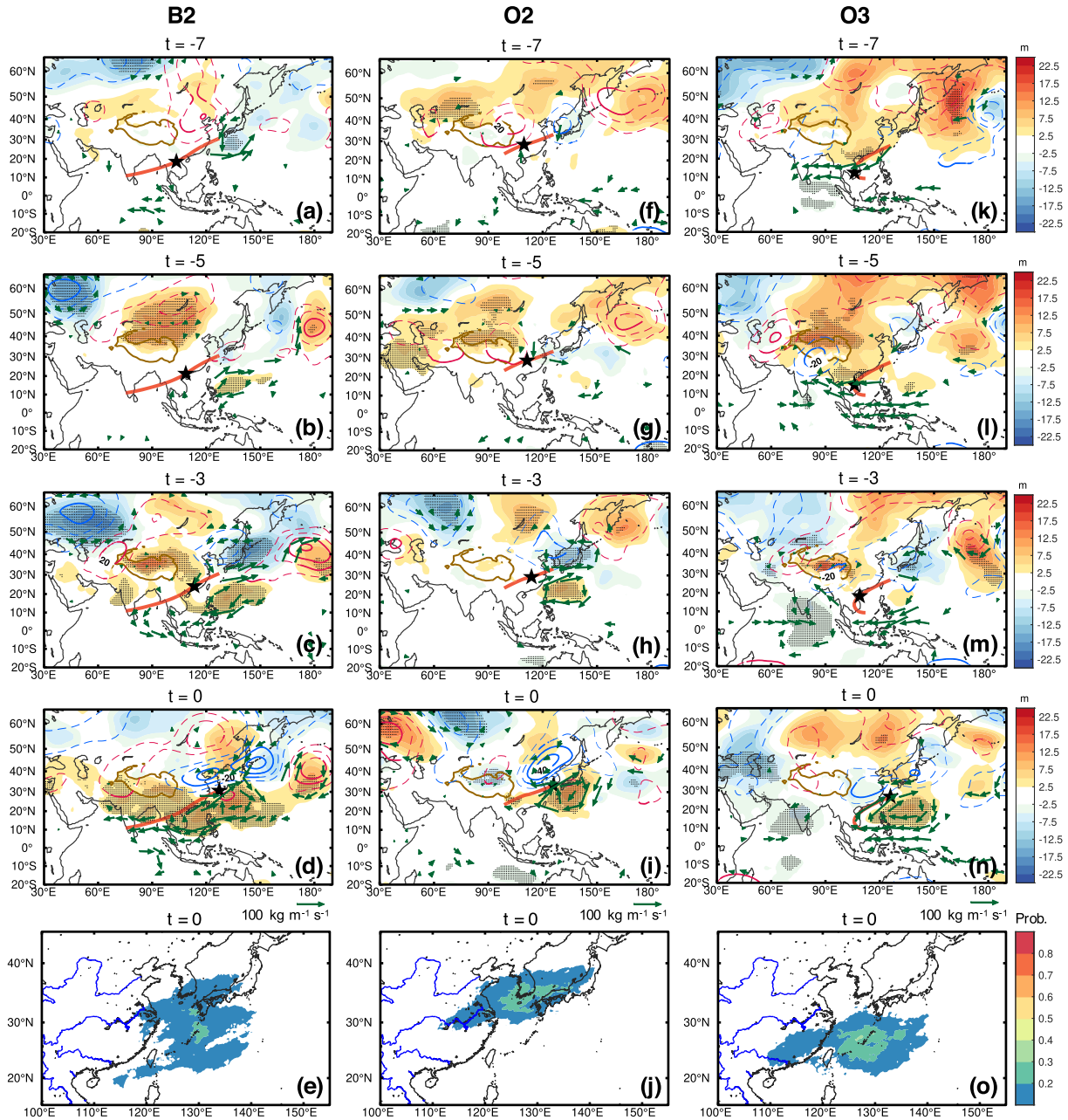

Fig. 5 Composites of meteorological fields within 2 weeks ahead of the clustered events fed by the B2, O2, and O3 channels. a–e As in Fig. 2, but for B2 (104 events), **f–j** O2 (108 events), and **k–o** O3 (69 events) on day −7, −5, −3, and 0.

pattern, we observe a standalone anticyclone drawing moisture from the southwest while propagating westward (e.g., Fig. 5b, h, l). The anticyclone occurs 5 days before the events, while we do not find coherent weather regimes beyond a 5-day lead time. This may suggest a rather short window of time for possible forecasting on rain belts associated with the above channels.

We again find the peak arrival timing helpful when interpreting the differences in the scale and location of the WNPSH. As the O3 channel mainly appears from April to May (Fig. 1f), it coincides with the time when the WNPSH mainly resides in the South China Sea[47] and thereby confines the rain belts in the south (Fig. 5l–o). Progressing into June, the WNPSH strengthens and hovers over South China and the entire Philippine Sea. At this stage, the WNPSH is capable of steering moisture from a farther region from the Bay of Bengal and thereby opening the B2 channel (Fig. 5b–d). In late summer when the WNPSH weakens and migrates slightly to the north, a much shorter O2 channel is formed to supply the rain belts over the Korean Peninsula and South Japan (Fig. 5h–j). These observations explain how the westward extension of the WNPSH in different monsoon stages modulates the rain belts' atmospheric water cycle, and thereby affecting summer rainfall variability in East Asia, as reported in many other studies[7,39,47–49].

Circumglobal wave trains

As extratropical Rossby wave trains were known to influence rainfall in the subtropical and mid-latitude regions[4,34,50], it might not be surprising that wave trains could also modulate some moisture channels for rain belts. Here, we identify two circumglobal wave trains (CGTs) 2 weeks ahead based on the wave activity analysis (see "Methods" section). The observed CGTs contribute to

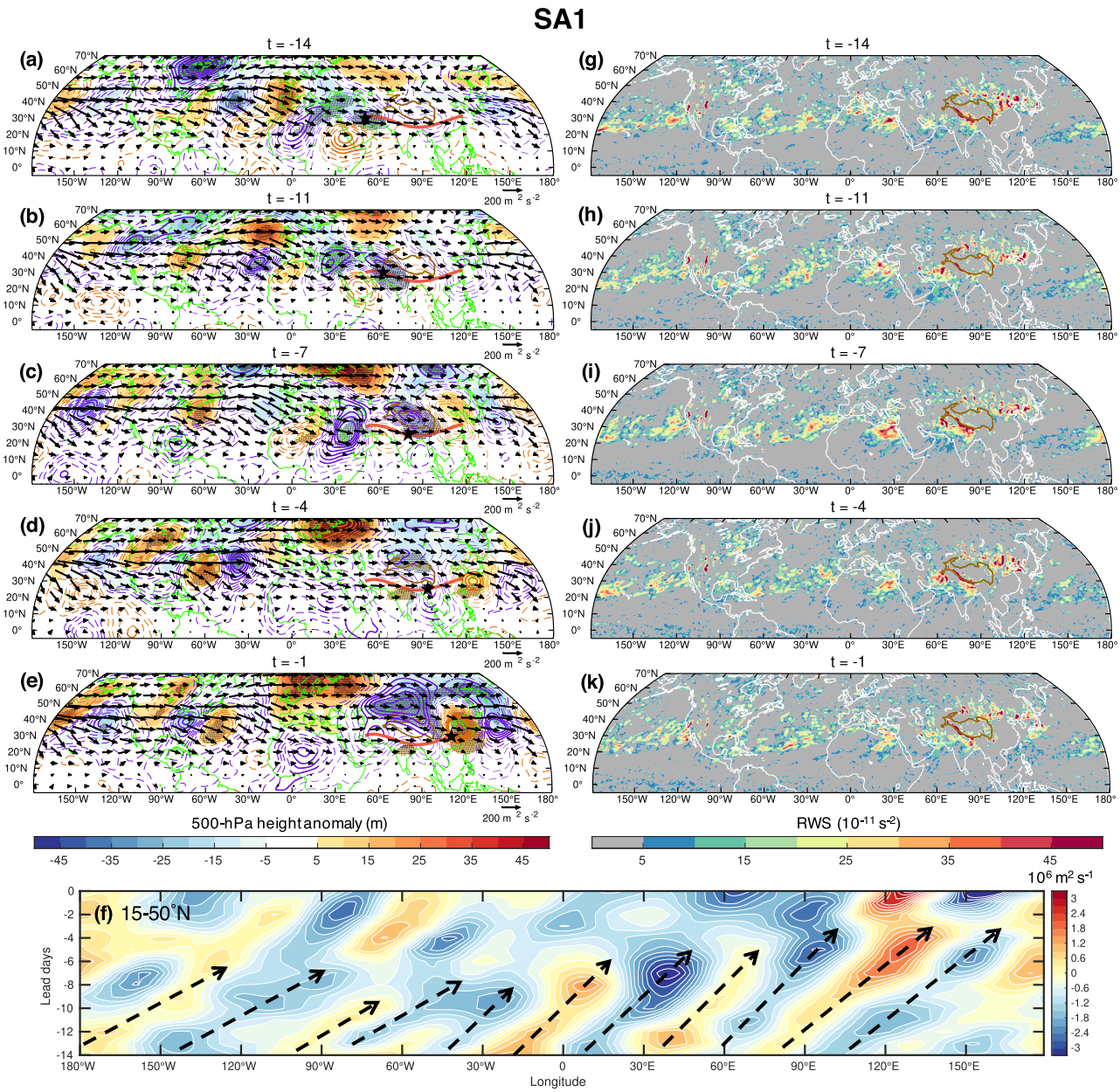

Fig. 6 Composites of wave activities and sources 2 weeks ahead of the rain belt events fed by the SA1 channel. a–e Composites of the 200-hPa wave activity fluxes (vector, unit: $m^2\ s^{-2}$), anomalous 500-hPa geopotential height (shading, unit: m) and the 200-hPa perturbation streamfunction (contour, interval: $4 \times 10^5\ m^2\ s^{-1}$) from day −14 to −1. Contours in orange (purple) denote positive (negative) values. The solid red line represents the regressed moisture channel for the cluster, and the black star denotes the moist air column's position along the regressed channel. Black dots over the shading and thick contours denote statistically significant values at the 0.05 level (Student's *t*-test). **f** Time-longitude plot of the meridionally averaged (15–50°N) 200-hPa perturbation streamfunction (shading, unit: $10^6\ m^2\ s^{-1}$). The dashed arrows guide the propagation of the wave peaks. **g–k** The Rossby wave source (RWS) (shading, unit: $10^{-11}\ s^{-2}$) from day −14 to −1.

the formation of several moisture channels by influencing the lower-level circulations.

One of the CGTs is notable since the initiation of the SA1 channel, which concatenates the upper-level circulations at the subtropics around the globe (Fig. 6a). One important feature of this CGT is that it covers both the Sahara Desert and the Middle East as the wave route penetrates to about 15°N the southmost (Fig. 6c). For this reason, it is much different from other well-documented wave trains such as the Silk Road pattern[51] or the Europe-China pattern[52]. By averaging the latitudinal band of 15–50°N in the 200-hPa perturbation streamfunction, it is clear that this CGT is guided by the upper-level westerly jet and propagates eastward from day −14 onwards (Fig. 6f). Meanwhile, the eastward-propagating CGT carries a deep trough in South Asia (60–90°E), which acts to steer the SA1 channel to the east till day −7 (Fig. 6a–c, f). Subsequent to that, an upper-level anticyclone reaches South Asia and contributes to the formation of the anticyclone at lower-levels (Fig. 6c–e), forming the dual-anticyclone pattern as discussed earlier (Fig. 3b, c). These interesting observations suggest the predominance of the upper-level wave train in regulating the lower-level circulations and thereby the SA1 channel.

Given such a well-organized CGT with the teleconnection to the SA1 channel, it is of interest to understand its origin. In the diagnosis

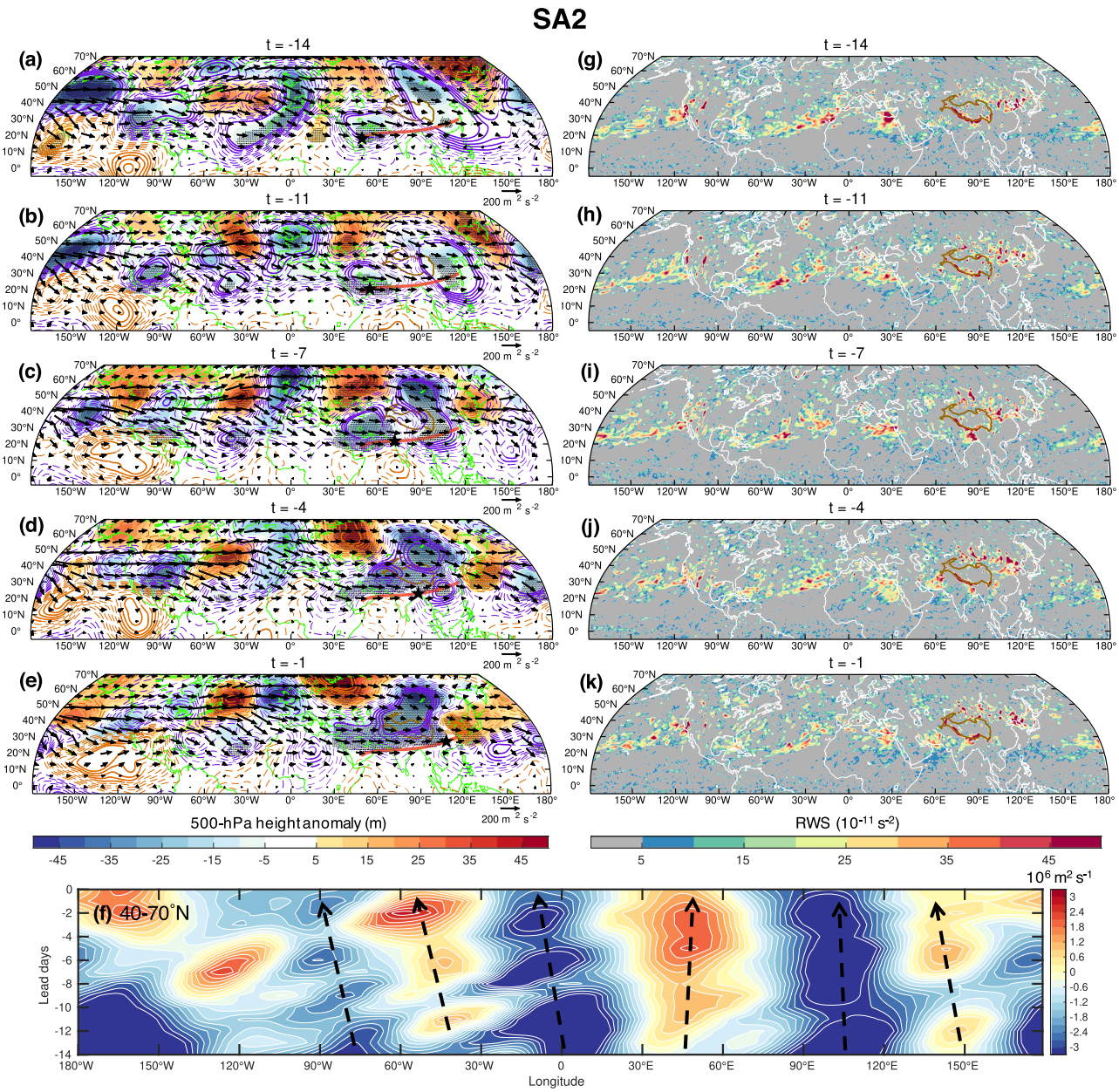

Fig. 7 Composites of wave activities and sources 2 weeks ahead of the rain belt events fed by the SA2 channel. a–k As in Fig. 6, but for the SA2 channel. The time-longitude plot in **f** shows the 200-hPa perturbation streamfunction (shading, unit: 10^6 m^2 s^{-1}) averaged meridionally at 40–70°N.

of the Rossby wave source[53] (RWS; see "Methods" section), strong wave sources are detected at nearly all longitudes, covering the central North Pacific, the Rocky Mountains, the North Atlantic, the Sahara Desert, South Asia, and North China (e.g., Fig. 6g). In particular, we observe prominent wave sources in the Sahara Desert and the Indian subcontinent since day −14 (Fig. 6g–k), which explains the southward shift of wave train to the subtropical deserts (e.g., Fig. 6c). Hence, we hereafter term this subtropical CGT as the Pacific–Atlantic–Saharan–Indian (PASI) pattern.

It is noteworthy that the wave sources mainly come from the vortex stretching term (Eq. (4)), whereas the vorticity advection term is almost negligible (results not shown). Thus, it is likely that the Saharan wave source results from descent motions over the arid regions due to radiative cooling[51], while the wave sources over oceans are often associated with subtropical highs (results not shown). We notice that the PASI pattern appears only in the SA1 and 2 channels (to be shown next), both of which mainly occur in April to mid-May (Fig. 1f). Taken together, the PASI pattern characterizes a springtime wave train induced by a stronger radiative cooling in both the Sahara and the Indian subcontinent from March through May[54], plus more intense upper-level westerlies compared to summer months. In addition, there might be a second CGT in the mid-latitudes after day −4 (Fig. 6d, e), which highly resembles a stationary CGT to be discussed later.

Likewise, we observe the PASI wave pattern alongside the SA2 channel 2 weeks ago (Fig. 7a), which features the canonical wave source in the Sahara Desert (Fig. 7g, h). While the PASI pattern is likely to initiate a deep trough in the Middle East to steer the lower-level moisture pathway, it appears short-lived and does not propagate to the east as it does in the previous case. Instead, there is another CGT in the mid-latitudes that dominates the weather regime since day −14. This CGT characterizes an arc path covering

the North Atlantic Ocean and Russia (Fig. 7b–d), and it becomes even more prominent when approaching the arrival of rain belt events (Fig. 7e). For convenience, we name such a CGT as the North Atlantic–Russian (NAR) pattern. In terms of the RWS, the North Atlantic wave source appears stronger and extends poleward (e.g., Fig. 7h), while the one over the Indian subcontinent appears weaker compared to the previous case (e.g., Figs. 6i and 7i). These observations may explain the short-lived PASI pattern and the dominance of the mid-latitude NAR pattern.

It also turns out that the NAR wave train is largely stationary, albeit with some slightly drifting wave peaks (Fig. 7f). For this reason, it keeps a long-standing deep trough over Siberia, which later penetrates southward and merges the South Asian trough (Fig. 7c, d). The influence of the resultant large-scale trough over the Asian continent is two-fold. On the one hand, it guides the inland moisture channel from South Asia to East Asia; on the other hand, it advects vorticity and cold-and-dry airmasses that both facilitate the frontogenesis to develop rain belt events in East Asia. Despite the circulation anomalies in the mid-troposphere and upper-troposphere associated with the NAR pattern are mostly consistent (Fig. 7a–e), we notice a westward tilt in the vertical axis between the 200-hPa and 850-hPa cyclonic circulations over Siberia since day −7 (Supplementary Fig. 4b, c). This observation infers a baroclinic instability that intensifies the Siberian trough according to the quasi-geostrophic theory[55].

It is interesting to see that the NAR pattern also pre-exists in the B3 and O1's weather regimes. Yet, the NAR pattern associated with the B3 channel is much weaker (Supplementary Fig. 5a–f), while the mid-latitude channel (O1) is governed by a reversed NAR pattern (Supplementary Fig. 6a–f). Noticeably, the O1 channel directs eastward even along the southern flank of the anomalous anticyclone in Siberia, which implies the predominance of the mid-latitude westerlies in the background. As the NAR pattern continues to strengthen, it gives rise to an anomalous cyclone in eastern Siberia (Supplementary Fig. 6c–f), which steers the latter part of the O1 pathway and facilitates the lower-level convergence for rain belt formation in the mid-latitudes (Supplementary Fig. 4m–o).

DISCUSSION

The overarching goal of this work is to unearth the dominant moisture channels for the EASM rain belt events and improve the knowledge about the pre-existing weather systems at lead times up to 2 weeks. Our findings, to some extent, challenge the traditional perception of moisture corridors for EASM rainfall from the Indian Ocean, South China Sea, western north Pacific, and Eurasia[3,14,24,25,28]. Based on the trajectory clustering, we obtain 15 moisture channels in four corridors, including the Somali, South Asian, Bay of Bengal, and the Pacific corridors. In particular, the Somali and South Asian corridors turn out to be crucial for supplying moisture to East Asian rain belts, but received less attention in the literature. Our results also update the knowledge pertaining to the minor role of the moisture channels from Eurasia and the South China Sea, as well as the absence of a cross-equatorial channel from Australia for East Asian rain belts.

The importance of terrestrial sources on the downwind continental precipitation gains increasing attention recently[13,15,29]. Here, we add that nearly half of the moisture channels to East Asian rain belts collect moisture mainly from terrestrial sources. Plus, we see a substantial number of rain belt events with moderate strength and persistence rely on terrestrial moisture supply (i.e., the South Asian corridor). In addition, if the long-range oceanic moisture channels are still present in a warmed climate, we would expect more extreme rain belt events due to the increase in both the water-holding capability of the atmosphere[56] and the evaporation over oceans[57] that fuel the moisture channels aloft.

Our results highlight several key weather systems that pave the moisture channels. In particular, the SAL-WNPSH coupling establishes the long-range Somali channels for the Pre-Meiyu and Meiyu rain belts, which pose hydrologic risks to South China and the mid-lower Yangtze river basin. By contrast, the interplay of two anticyclones in South Asia and the western North Pacific explains the South Asian moisture channels in early-summer and mid-summer. Similar signals for the SAL-WNPSH coupling and the dual-anticyclone pattern were also noted in our previous study based on correlation maps of the meteorological fields with moisture contributions from the Arabian Sea and the Indian subcontinent[13]. Here, we again observe these interesting weather patterns and examine their controls on the moisture channels in greater detail. We argue that the upper-level divergent winds originated from the SAL could contribute to the later development of the WNPSH and thereby explain their coupling. Other essential weather regimes look familiar to us, including tropical cyclones and the zonal oscillation of the WNPSH[39,48,49], which steer a number of moisture channels from the Pacific basin, Bay of Bengal, and regions in the vicinity.

The most interesting finding perhaps lies in the interaction between global wave trains and regional circulations, as manifested by the two CGTs that influence the moisture channels for East Asian rain belts. One is the springtime PASI pattern that propagates eastward and passes by the Sahara, the Middle East, and the Indian subcontinent. This wave train carries a South Asian trough that steers a South Asian channel. Another is the NAR pattern that is more common in several moisture channels, which modulates the synoptic-scale weather regime over Siberia to facilitate moisture tracks and the rain belt formation. It is worth mentioning that the NAR pattern considerably resembles the Russia–China pattern found in our previous study on summertime precipitation in eastern China[4], which may suggest the crucial role of the NAR pattern in the East Asian warm season.

Taking into account the average lifetime of moisture in the atmosphere[58], we limit our analysis to 2 weeks prior to the rain belt events for exploring the essential weather regimes. There could be additional drivers across a broader spectrum of time scales that influence the moisture channels. Teleconnections and climatic forcings at longer time scales, such as the 30–60-day boreal summer intraseasonal oscillation (BSISO[59], which has a mode that resembles the SAL-WNPSH coupling), the El Niño–Southern Oscillation[60–62], the North Atlantic Oscillation[63], the Arctic sea ice variations[64], and global warming[11,65], have known to affect the East Asian rainfall variability. How these slowly varying forcings and oscillations interact with the moisture channels to the East Asian rain belts is worth investigating in the future. The CGTs discovered in this study may link with the summertime Rossby wave breaking[51,66] that warrants further research. We also look forward to future studies on the predictive skills of the discovered weather regimes before the rain belts.

With a more holistic picture of the dominating moisture channels, the key weather patterns and the teleconnections within a 2-week lead time, findings from this work would help better understand the hydrologic cycle of rain belts and benefit weather diagnosis, numerical model evaluation, and short-term heavy rainfall forecasting in East Asia.

METHODS

Data

Meteorological variables are retrieved from the fifth generation of the European Center for Medium-Range Weather Forecast (ECMWF) atmospheric reanalysis data (ERA5) between 1981 and 2018 at 1° grid resolution for diagnoses[67]. ERA5 data with a higher spatial resolution (0.25° × 0.25°) is adopted as the input for the moisture tracking model. Best track data from the Hong Kong Observatory in the International Best

Track Archive for Climate Stewardship (IBTrACS) is adopted for tracking tropical cyclones[68,69].

Dynamical recycling model (DRM)

We employ the semi-Lagrangian DRM[35,70] to perform moisture backtracking. It has been adopted to derive the contributions from local or external sources in different monsoon regions with reasonable results at a low computational demand[13,20,70,71]. The recycling ratio R in the DRM represents the fraction of precipitation in a sink grid recycled from a source's evapotranspiration along the backward trajectory. It can be computed analytically with a semi-Lagrangian scheme[35]:

$$R(x,y,t) = 1 - \exp\left[-\int_0^{\tau} \frac{E(x',y',t')}{W(x',y',t')}\mathrm{d}\tau'\right], \quad (1)$$

where E and W are evapotranspiration and precipitable water in the semi-Lagrangian coordinate (x', y', t'), respectively. This equation is also equivalent to the sum of the relative contribution from each source along the trajectory[70]. Following our previous work[13], we prescribe 30 source regions within a model domain of 20°S–65°N, 30–190°E (Supplementary Fig. 1) to construct the source-receptor network for each rain belt. The backward tracking algorithm is performed at a 10-min time interval and stops once the tracking time exceeds 14 days, or the trajectory reaches the domain boundaries. The 14-day tracking time is comparable to the mean residence time of atmospheric moisture in East and South Asia[58].

EASM rain belt events detection

We detect rain belts within the East Asian monsoon domain (15–45°N, 105–145°E) from April through September in 1981–2018 based on the following criteria. First, the rainfall amount at each 1° grid cell needs to be greater than its local threshold, which is the smoothed 80th percentile of the wet day precipitation (>1 mm day^{-1}) by the Gaussian kernel smoothing. By connecting the heavy rainfall grids from eight directions with no gaps allowed, a rain belt is detected if its zonal extent is greater than 10° of longitude.

Here, we present the idea of assigning rain belts to the same event if they are fed by similar sources. For any pair of rain belts occurring on consecutive days, they are deemed the same event if the Euclidean distance D in the recycling ratios of their source–receptor networks is less than 10%. Namely,

$$D(R_i,\ R_j) = \sqrt{\sum_{l=1}^{n=30}\left[R_i(l) - R_j(l)\right]^2} < 10\%,\ \textit{for } i \neq j, \quad (2)$$

where R_i and R_j are the arrays containing the 30 sources' recycling ratios (in %) for the pair of rain belts. We set the threshold in D to be 10% as it refers to the level after the peak in the distribution based on all pairs of rain belts (Supplementary Fig. 7). All individual rain belts are assigned to an event with the smallest D (i.e., having the most similar source-receptor network). We obtain up to 1265 high-impact rain belt events for analysis, each having at least one rain belt with over 90% of it in a nested monsoon domain of 20–40°N, 110–140°E[1]. Examples of the detected events are given in Supplementary Fig. 8 for readers' reference.

Trajectory clustering

Based on our preliminary analysis, the East Asian rain belt events are supplied by several moisture supply channels (e.g., Supplementary Fig. 8b, d). As such, we employ an Expectation–Maximization (EM)-based curve clustering algorithm[72] to classify the DRM-derived moisture trajectories from the first rain belt affecting the EASM domain in all events. A 4th order polynomial regression model is trained in the curve clustering. The optimal number of clusters is selected to be 15, at which the gradient of the trained likelihood becomes small and fluctuated (Supplementary Fig. 9). Despite the same gradient of likelihood when using 13 or 15 clusters, the results based on 15 clusters generally produce a cleaner and more reasonable clustering compared to that using 13 clusters, as illustrated in Supplementary Fig. 10. Finally, we assign a rain belt event to a trajectory cluster if over 30% of the first rain belt's back trajectories affecting the EASM domain belong to that cluster. We leave only 7% of the events without cluster membership and 21% with two or more memberships through this way.

Wave activity analysis

The wave activity flux $\mathbf{W}$ (m^2 s^{-2}) for stationary Rossby wave on a pressure level[73] can be computed by

$$\mathbf{W} = \frac{1}{2|\overline{\mathbf{U}}|}\begin{bmatrix} \overline{u}\left(\psi_x'^2 - \psi'\psi'_{xx}\right) + \overline{v}\left(\psi'_x\psi'_y - \psi'\psi'_{xy}\right) \\ \overline{u}\left(\psi'_x\psi'_y - \psi'\psi'_{xy}\right) + \overline{v}\left(\psi_y'^2 - \psi'\psi'_{yy}\right) \end{bmatrix}, \quad (3)$$

where $\overline{\mathbf{U}} = (\overline{u}, \overline{v})$ is the climatological wind velocities (m s^{-1}) and ψ' the perturbation streamfunction (m^2 s^{-1}) from the climatological state. The subscript denotes partial derivative.

We are also interested in the Rossby wave source (RWS, s^{-2}), which can be quantified by[53]:

$$RWS = -\eta D - \mathbf{v}_\chi \cdot \nabla\eta, \quad (4)$$

where $\mathbf{v}_\chi$ is the divergent wind (m s^{-1}), η is the absolute vorticity (s^{-1}), and D the divergence of wind (s^{-1}). As such, the RWS is contributed by the rate of change of vorticity due to vortex stretching (i.e., $-\eta D$) and the vorticity advection by $\mathbf{v}_\chi$. Both the wave source and the wave activity fluxes are computed on spectral harmonics. We select the 200-hPa pressure level for investigation as wave sources generally peak at this level[74].

Statistical significance

A two-tailed one-sample Student's t-test with a significance level of 0.05 is adopted to assess the statistical significance of the meteorological field anomalies shown in the composite maps (e.g., Figs. 2–7). The t-test is performed with the null hypothesis that the anomalies come from a t-distribution with a mean equal to zero and unknown variance.

DATA AVAILABILITY

The meteorological data is retrieved from the ERA5 by the European Center for Medium-Range Weather Forecast (ECMWF) at https://www.ecmwf.int/en/forecasts/datasets/reanalysis-datasets/era5. The IBTrACS best track data can be accessed from https://www.ncdc.noaa.gov/ibtracs/index.php?name=ib-v4-access. Derived data supporting the findings of this study are available from the corresponding author upon reasonable request.

CODE AVAILABILITY

The source code for the DRM can be accessed by https://github.com/huancui/DRM_2LDRM.

Received: 8 January 2021; Accepted: 30 April 2021;
Published online: 28 May 2021

REFERENCES

1. Ding, Y. & Chan, J. C. L. The East Asian summer monsoon: an overview. *Meteorol. Atmos. Phys.* **89**, 117–142 (2005).
2. Chiang, J. C. H., Swenson, L. M. & Kong, W. Role of seasonal transitions and the westerlies in the interannual variability of the East Asian summer monsoon precipitation. *Geophys. Res. Lett.* **44**, 3788–3795 (2017).
3. Tao, S. & Chen, L. In *Monsoon Meteorology* (eds. Chang, C. -P. & Krishnamurti, T. N.) 60–92 (Oxford University Press, 1987).
4. Dai, L., Cheng, T. F. & Lu, M. Summer monsoon rainfall patterns and predictability over Southeast China. *Water Resour. Res.* **56**, 1–21 (2020).
5. Xu, W., Zipser, E. J. & Liu, C. Rainfall characteristics and convective properties of Mei-Yu precipitation systems over South China, Taiwan, and the South China sea. Part I: TRMM observations. *Mon. Weather Rev.* **137**, 4261–4275 (2009).
6. Li, H., Hu, Y., Zhou, Z., Peng, J. & Xu, X. Characteristic features of the evolution of a Meiyu frontal rainstorm with Doppler radar data assimilation. *Adv. Meteorol.* **2018**, 1–17 (2018).
7. Akiyama, T. The large-scale aspects of the characteristic features of the Baiu front. *Pap. Meteorol. Geophys.* **24**, 157–188 (1973).
8. Du, Y., Zhang, Q., Ying, Y. & Yang, Y. Characteristics of low-level jets in Shanghai during the 2008–2009 warm seasons as Inferred from wind profiler radar data. *J. Meteorol. Soc. Jpn* **90**, 891–903 (2012).
9. Yao, X., Ma, J., Zhang, D.-L. & Yan, L. A 33-yr Meiyu-season climatology of shear lines over the Yangtze-Huai river basin in Eastern China. *J. Appl. Meteorol. Climatol.* (2020).
10. Tomita, T., Yamaura, T. & Hashimoto, T. Interannual variability of the Baiu season near Japan evaluated from the equivalent potential temperature. *J. Meteorol. Soc. Jpn* **89**, 517–537 (2011).

11. Chiang, J. C. H., Fischer, J., Kong, W. & Herman, M. J. Intensification of the Pre-Meiyu Rainband in the late 21st century. *Geophys. Res. Lett.* **46**, 7536–7545 (2019).
12. Park, H. S., Chiang, J. C. H. & Bordoni, S. The mechanical impact of the Tibetan Plateau on the seasonal evolution of the South Asian monsoon. *J. Clim.* **25**, 2394–2407 (2012).
13. Cheng, T. F. & Lu, M. Moisture source-receptor network of the East Asian summer monsoon land regions and the associated atmospheric steerings. *J. Clim.* **33**, 9213–9231 (2020).
14. Sun, B. & Wang, H. Analysis of the major atmospheric moisture sources affecting three sub-regions of East China. *Int. J. Climatol.* **35**, 2243–2257 (2015).
15. Fremme, A. & Sodemann, H. The role of land and ocean evaporation on the variability of precipitation in the Yangtze River valley. *Hydrol. Earth Syst. Sci.* **23**, 2525–2540 (2019).
16. Pan, M. & Lu, M. A novel atmospheric river identification algorithm. *Water Resour. Res.* **55**, 6069–6087 (2019).
17. Pan, M. & Lu, M. East Asia atmospheric river catalog: annual cycle, transition mechanism, and precipitation. *Geophys. Res. Lett.* **47**, e2020GL089477 (2020).
18. Volosciuk, C. et al. Rising mediterranean sea surface temperatures amplify extreme summer precipitation in central europe. *Sci. Rep.* **6**, 1–7 (2016).
19. Gimeno, L. et al. Recent progress on the sources of continental precipitation as revealed by moisture transport analysis. *Earth Sci. Rev.* **201**, 103070 (2020).
20. Hu, H. & Dominguez, F. Evaluation of oceanic and terrestrial sources of moisture for the North American monsoon using numerical models and precipitation stable isotopes. *J. Hydrometeorol.* **16**, 19–35 (2015).
21. Lu, M. & Hao, X. Diagnosis of the tropical moisture exports to the mid-latitudes and the role of atmospheric steering in the extreme precipitation. *Atmosphere* **8**, 256 (2017).
22. Wei, J., Dirmeyer, P. A., Bosilovich, M. G. & Wu, R. Water vapor sources for Yangtze River Valley rainfall: climatology, variability, and implications for rainfall forecasting. *J. Geophys. Res. Atmos.* **117**, 1–11 (2012).
23. Wang, N. et al. Quantitative diagnosis of moisture sources and transport pathways for summer precipitation over the mid-lower Yangtze River Basin. *J. Hydrol.* **559**, 252–265 (2018).
24. Shi, Y., Jiang, Z., Liu, Z. & Li, L. A Lagrangian analysis of water vapor sources and pathways for precipitation in East China in different stages of the East Asian summer monsoon. *J. Clim.* **33**, 977–992 (2020).
25. Chow, K. C., Tong, H. W. & Chan, J. C. L. Water vapor sources associated with the early summer precipitation over China. *Clim. Dyn.* **30**, 497–517 (2008).
26. Simmonds, I., Bi, D. & Hope, P. Atmospheric water vapor flux and its association with rainfall over China in summer. *J. Clim.* **12**, 1353–1367 (1999).
27. Zhou, T. J. & Yu, R. C. Atmospheric water vapor transport associated with typical anomalous summer rainfall patterns in China. *J. Geophys. Res. D Atmos.* **110**, 1–10 (2005).
28. Ding, Y. In *East Asian Monsoon* (ed. Chang, C.-P.) 3–53 (World Scientific Publishing Co., 2004).
29. Wang-Erlandsson, L. et al. Remote land use impacts on river flows through atmospheric teleconnections. *Hydrol. Earth Syst. Sci.* **22**, 4311–4328 (2018).
30. Shrestha, D. L., Robertson, D. E., Wang, Q. J., Pagano, T. C. & Hapuarachchi, H. A. P. Evaluation of numerical weather prediction model precipitation forecasts for short-term streamflow forecasting purpose. *Hydrol. Earth Syst. Sci.* **17**, 1913–1931 (2013).
31. Kang, S. D., Shin, D. W., Cocke, S., Kim, H. D. & Jung, W. S. Comparison of ensemble methods for summer-time numerical weather prediction over East Asia. *Meteorol. Atmos. Phys.* **113**, 27–38 (2011).
32. Richard, E. et al. Intercomparison of mesoscale meteorological models for precipitation forecasting. *Hydrol. Earth Syst. Sci.* **7**, 799–811 (2003).
33. Arakawa, A. In *The Representation of Cumulus Convection in Numerical Models* 1–15 (American Meteorological Society, 1993).
34. Lu, M., Lall, U., Schwartz, A. & Kwon, H. Precipitation predictability associated with tropical moisture exports and circulation patterns for a major flood in France in 1995. *Water Resour. Res.* **49**, 6381–6392 (2013).
35. Dominguez, F. et al. Impact of atmospheric moisture storage on precipitation recycling. *J. Clim.* **19**, 1513–1530 (2006).
36. Martinez, J. A., Dominguez, F., Martinez, J. A. & Dominguez, F. Sources of atmospheric moisture for the La Plata river basin*. *J. Clim.* **27**, 6737–6753 (2014).
37. He, J., Ju, J., Wen, Z., Lü, J. & Jin, Q. A review of recent advances in research on Asian monsoon in China. *Adv. Atmos. Sci.* **24**, 972–992 (2007).
38. Webster, P. J. In *Monsoons* 3–32 (Wiley, 1987).
39. Cheng, T. F., Lu, M. & Dai, L. The zonal oscillation and the driving mechanisms of the extreme western North Pacific subtropical high and its impacts on East Asian summer precipitation. *J. Clim.* **32**, 3025–3050 (2019).
40. Keys, P. W., Barnes, E. A., Van Der Ent, R. J. & Gordon, L. J. Variability of moisture recycling using a precipitationshed framework. *Hydrol. Earth Syst. Sci.* **18**, 3937–3950 (2014).
41. Van Der Ent, R. J., Savenije, H. H. G., Schaefli, B. & Steele-Dunne, S. C. Origin and fate of atmospheric moisture over continents. *Water Resour. Res.* **46**, 1–12 (2010).
42. Dominguez, F., Hu, H. & Martinez, J. A. Two-layer dynamic recycling model (2L-DRM): learning from moisture tracking models of different complexity. *J. Hydrometeorol.* **21**, 3–16 (2020).
43. Dai, L., Cheng, T. F. & Lu, M. Define East Asian monsoon annual cycle via a self-organizing map-based approach. *Geophys. Res. Lett.* **48**, e2020GL089542 (2021).
44. Tian, S.-F. & Yasunari, T. Climatological aspects and mechanism of spring persistent rains over Central China. *J. Meteorol. Soc. Jpn Ser. II* **76**, 57–71 (1998).
45. Chang, C.-P. & Chen, G. T. J. Tropical circulations associated with Southwest Monsoon onset and westerly surges over the South China sea. *Mon. Weather Rev.* **123**, 3254–3267 (1995).
46. Krishnamurti, T. N., Stefanova, L. & Misra, V. *Tropical Meteorology: An Introduction* (Springer, 2013).
47. Chang, C.-P., Zhang, Y. & Li, T. Interannual and interdecadal variations of the East Asian Summer monsoon and tropical Pacific SSTs. Part I: roles of the subtropical ridge. *J. Clim.* **13**, 4310–4325 (2000).
48. Ren, X., Yang, X. Q. & Sun, X. Zonal oscillation of Western Pacific subtropical high and subseasonal SST variations during Yangtze persistent heavy rainfall events. *J. Clim.* **26**, 8929–8946 (2013).
49. Mao, J., Sun, Z. & Wu, G. 20-50-day oscillation of summer Yangtze rainfall in response to intraseasonal variations in the subtropical high over the western North Pacific and South China Sea. *Clim. Dyn.* **34**, 747–761 (2010).
50. Suzuki, S. I. & Hoskins, B. The large-scale circulation change at the end of the Baiu season in Japan as seen in ERA40 data. *J. Meteorol. Soc. Jpn* **87**, 83–99 (2009).
51. Enomoto, T., Hoskins, B. J. & Matsuda, Y. The formation mechanism of the Bonin high in August. *Q. J. R. Meteorol. Soc.* **129**, 157–178 (2003).
52. Chen, G. & Huang, R. Excitation mechanisms of the teleconnection patterns affecting the July precipitation in Northwest China. *J. Clim.* **25**, 7834–7851 (2012).
53. Sardeshmukh, P. D. & Hoskins, B. J. The generation of global rotational flow by steady idealized tropical divergence. *J. Atmos. Sci.* **45**, 1228–1251 (1988).
54. Webster, P. J. et al. Monsoons: processes, predictability, and the prospects for prediction. *J. Geophys. Res. Ocean.* **103**, 14451–14510 (1998).
55. Holton, J. R. & Hakim, G. J. In *An Introduction to Dynamic Meteorology* vol. 9780123848 1–532 (Academic Press, 2012).
56. Trenberth, K. E., Dai, A., Rasmussen, R. M. & Parsons, D. B. The changing character of precipitation. *Bull. Am. Meteorol. Soc.* **84**, 1205–1217 (2003).
57. Gimeno, L., Nieto, R. & Sorí, R. The growing importance of oceanic moisture sources for continental precipitation. *npj Clim. Atmos. Sci.* **3**, 1–9 (2020).
58. van der Ent, R. J. & Tuinenburg, O. A. The residence time of water in the atmosphere revisited. *Hydrol. Earth Syst. Sci.* **21**, 779–790 (2017).
59. Lee, J.-Y. et al. Real-time multivariate indices for the boreal summer intraseasonal oscillation over the Asian summer monsoon region. *Clim. Dyn.* **40**, 493–509 (2013).
60. Wang, B., Wu, R. & Fu, X. Pacific–East Asian teleconnection: How does ENSO affect East Asian climate? *J. Clim.* **13**, 1517–1536 (2000).
61. Wang, B., Xiang, B. & Lee, J.-Y. Subtropical high predictability establishes a promising way for monsoon and tropical storm predictions. *Proc. Natl Acad. Sci. USA* **110**, 2718–2722 (2013).
62. Stuecker, M. F. et al. Combination mode dynamics of the anomalous Northwest Pacific anticyclone. *J. Clim.* **28**, 1093–1111 (2015).
63. Wu, Z., Wang, B., Li, J. & Jin, F. F. An empirical seasonal prediction model of the east Asian summer monsoon using ENSO and NAO. *J. Geophys. Res. Atmos.* **114**, 1–13 (2009).
64. Wu, B., Zhang, R. & Wang, B. On the association between spring Arctic sea ice concentration and Chinese summer rainfall: a further study. *Adv. Atmos. Sci.* **26**, 666–678 (2009).
65. Sooraj, K. P., Terray, P. & Mujumdar, M. Global warming and the weakening of the Asian summer monsoon circulation: assessments from the CMIP5 models. *Clim. Dyn.* **45**, 233–252 (2015).
66. Samanta, D., Dash, M. K., Goswami, B. N. & Pandey, P. C. Extratropical anticyclonic Rossby wave breaking and Indian summer monsoon failure. *Clim. Dyn.* **46**, 1547–1562 (2016).
67. Copernicus Climate Change Service. ERA5: Fifth generation of ECMWF atmospheric reanalyses of the global climate. *Copernicus Climate Change Service Climate Data Store (CDS)* https://cds.climate.copernicus.eu/cdsapp#!/dataset/reanalysis-era5-single-levels?tab=overview (2017).
68. Knapp, K. R., Kruk, M. C., Levinson, D. H., Diamond, H. J. & Neumann, C. J. The international best track archive for climate stewardship (IBTrACS). *Bull. Am. Meteorol. Soc.* **91**, 363–376 (2010).
69. Knapp, K. R., Diamond, H. J., Kossin, J. P., Kruk, M. C. & Schreck, C. J. I. *International Best Track Archive for Climate Stewardship (IBTrACS) Project, Version 4*. [West Pacific]. (NOAA National Centers for Environmental Information, 2018).
70. Alejandro Martinez, J., Dominguez, F., Martinez, J. A. & Dominguez, F. Sources of atmospheric moisture for the La Plata River Basin. *J. Clim.* **27**, 6737–6753 (2014).

71. Pathak, A., Ghosh, S., Alejandro Martinez, J., Dominguez, F. & Kumar, P. Role of oceanic and land moisture sources and transport in the seasonal and interannual variability of summer monsoon in India. *J. Clim.* **30**, 1839–1859 (2017).
72. Gaffney, S. J. *Probabilistic Curve-Aligned Clustering and Prediction with Regression Mixture Models* (University of California, 2004).
73. Takaya, K. & Nakamura, H. A formulation of a phase-independent wave-activity flux for stationary and migratory quasigeostrophic eddies on a zonally varying basic flow. *J. Atmos. Sci.* **58**, 608–627 (2001).
74. Scaife, A. A. et al. Tropical rainfall, Rossby waves and regional winter climate predictions. *Q. J. R. Meteorol. Soc.* **143**, 1–11 (2017).
75. Pawlowicz, R. M. _Map: A Mapping package for Matlab. www.eoas.ubc.ca/~rich/map.html (2020).

ACKNOWLEDGEMENTS

This research contributes to, and is financially supported by the National Natural Science Foundation of China funded project (no. 51709051) and the Hong Kong Research Grants Council funded projects (nos. 16201218 & 16200920). The authors thank two anonymous reviewers for their helpful comments on the manuscript. The authors also thank Prof. Francina Dominguez and Dr. Huancui Hu for their generosity in offering the code of the DRM. Some figures in this paper are generated using a Matlab package "M_Map"[75].

AUTHOR CONTRIBUTIONS

T.F.C. and M.L. designed the study. D.L. performed the rain belt detection and prepared the data. T.F.C. conducted the moisture tracking experiments and the analyses. T.F.C. and M.L. wrote and revised the manuscript. All co-authors contributed to the discussion of the results.

COMPETING INTERESTS

The authors declare no competing interests.

ADDITIONAL INFORMATION

Supplementary information The online version contains supplementary material available at https://doi.org/10.1038/s41612-021-00187-6.

Correspondence and requests for materials should be addressed to M.L.

Reprints and permission information is available at http://www.nature.com/reprints

Publisher's note Springer Nature remains neutral with regard to jurisdictional claims in published maps and institutional affiliations.